Revista Brasileira de Geofísica
RBGf
Brazilian Journal of Geophysics

Revista Brasileira de Geofísica (2015) 33(3): 403-420
© 2015 Sociedade Brasileira de Geofísica
ISSN 0102-261X
www.scielo.br/rbg

# PROCESSING AND IMAGING OF MARINE SEISMIC DATA FROM THE JEQUITINHONHA BASIN (BAHIA, BRAZIL)

Lourenildo W.B. Leite[1], J. Mann[2] and Wildney W.S. Vieira[1]

**ABSTRACT.** The present study results from a consistent processing and imaging of marine seismic data from a set collected over sedimentary basins of the East Brazilian Atlantic. Our general aim is first to subsidize geological interpretations with plausible subsurface images for oil and gas exploration. In second place, to verify published schematic geological interpretation for these basins by underlying the sediment/basement contact, from where subvertical faults are projected upwards through the basin followed by folded structures. The data-driven results can be used to trace the reflector boundaries in the time sections, submitted to time-to-depth axis transformation, and to be used as a first model for further basin pressure prediction, where natural pumps necessarily develop for the mechanism of oil and gas accumulation. The applied fundamental techniques are mainly based on the data-driven common reflection surface stack, where it is shown the improvement of the signal-to-noise ratio, the lateral continuity of the reflection events, the resolution, and that time migration collapses the diffraction events. The CRS migration strongly collapsed the diffraction events, allowing some subsurface structures be more evident. The free surface and some shallow internal multiples can be clearly traced for further processing aiming at their attenuation. The interpretation lines are meant to show the geometry of selected reflectors, and to help comparing the results with other similar sections. One can trace some subvertical fault systems starting from the lower part of the section (interpreted as the basement), and their extension upwards through the sedimentary sequence.

**Keywords**: CRS stack, CRS migration, residual static correction, NIP wave tomography.

**RESUMO.** O presente artigo resulta de um processamento e imageamento consistentes de dados sísmicos marinhos de levantamento realizado em bacias sedimentares do Atlântico do Nordeste brasileiro. Nossos objetivos gerais são em primeiro lugar subsidiar as interpretações geológicas com imagens plausíveis do subsolo, e voltadas à exploração de óleo e gás. Em segundo lugar, verificar as interpretações geológicas esquemáticas publicadas para estas bacias, para conferir o delineamento do contato sedimento/embasamento, de onde falhas subvertical são projetadas através da bacia, seguidas de estruturas dobradas. Os resultados baseados em dados reais podem ser usados para delinear interfaces refletoras contidas nas seções tempo, submetidos à transformação da coordenada tempo para profundidade, e que podem ser usados posteriormente como um primeiro modelo para a predição de pressão em bacias sedimentares, onde se desenvolve um bombeamento natural necessário para a acumulação de óleo e gás. As técnicas fundamentais aplicadas baseiam-se principalmente no denominado empilhamento de superfície de reflexão comum, baseado em dados observados, onde se mostra a evolução da relação sinal-ruído, da continuidade lateral dos eventos de reflexão, da resolução, e o colapso dos eventos de difração nas seções de migração do tempo. A migração CRS colapsa fortemente os eventos de difração permitindo que algumas estruturas do subsolo sejam mais evidentes. Múltiplas da superfície livre, e algumas internas rasas, podem ser claramente traçadas para processamento adicional que visam a atenuação. As linhas de interpretação traçadas visam mostrar a geometria dos refletores selecionados, e ajudar na comparação com outros resultados de seções semelhantes. Pode-se traçar um sistema de falhas subvertical a partir da base inferior (interpretada como o embasamento) da seção escolhida como referência, e os seus prolongamentos através da sequência sedimentar.

**Palavras-chave**: empilhamento CRS, migração CRS, correção estática residual, tomografia NIP.

[1]Universidade Federal do Pará, Campus Universitário do Guamá, Instituto de Geociências, Rua Bernardo Sayão, s/n, 66075-110 Belém, PA, Brazil. Phone: +55(91) 3201-7693; Fax: +55(91) 3201-7609 – E-mail: lwbleite@gmail.com; wildneyvieira@gmail.com

[2]Karlsruhe Institute of Technology, Geophysical Institute, Hertzstr. 16, 76187 Karlsruhe, Germany – E-mail: Juergen.Mann@kit.de

## INTRODUCTION

Several authors, including Gomes et al. (2007), Heilmann et al. (2007), Leite et al. (2008) and Minato et al. (2012), have presented different case studies where the Common-Reflection-Surface (CRS) stack workflows have been applied to land datasets to obtain better structural images, as the classical works of Trappe et al. (2001) and Gierse et al. (2003). Due to the relevance of oil exploration, the present work represents an extension of these efforts to marine data collected over a specific sedimentary basin. The main steps of processing and imaging gave results that clearly show improvement on the continuity of reflection events, and an enhancement in the signal-to-noise ratio. Also, with the free surface multiples enhanced, it becomes convenient to have them underlined, and to apply further attenuation techniques. Prior to the CRS processing, several tasks were performed beginning with the geometry setup, muting of bad shot and receiver gathers, $f$-$x$ and $f$-$k$ filtering, semblance velocity analysis, multiple deconvolution.

Complex geological environments often pose severe difficulties for accurate imaging in time and depth domains, and even more if combined with complicate near surface conditions. Under such circumstances, where simple geometrical model assumptions may fail, it is of particular importance to extract (by parts) as much information as possible directly from the measured data.

The CRS stack methodology, that started being described by Müeller et al. (1998) and Mann (2002), among others, has become a powerful data-driven method for improving the zero-offset (ZO) simulation of seismic data. Although topography can be directly considered during the stack process, it was not required for the present data. For the 2D processing, every ZO sample is associated with three kinematic wavefield attributes which represent useful by-products of the stacking process (Hubral, 1999). These attributes have been applied to improve the stack itself, and to support subsequent processing as described in Gamboa (2003) and Koglin (2005), among others. Using the CRS attributes for the transformation time-to-depth domains, an advanced data processing workflow could be established, covering a broad range of seismic reflection imaging issues in a consistent manner (Duveneck, 2004).

NIP wave tomography takes part in the CRS technology as a technique to obtain a depth velocity distribution based on curve fitting between data and theoretical model for a number of $n_{\text{data}}$ observation points representing the parameters of the the Normal Incidence Point (NIP) wavefront at the surface, and picked on the CRS stack section. The aim is to find a model defined on a regular grid with velocity values $v_{jk}$, that can to be used in depth migration. The inversion process is classified as a typical mixed-determined problem. The object function was constructed as the deviation error between the observed and theoretical model in the least-squares sense, with the addition of constraints in the parameter model solution.

The marine data set for this case study was acquired for petroleum exploration, and our theme was basin reevaluation based on seismic reprocessing. We used non commercial software with the format established by Cohen & Stockwell (2005).

Cainelli & Mohriak (1999) and Mohriak et al. (2008) describe the geological sedimentary basins of the passive continental shelf of the Brazilian South Atlantic, where the rifts are directly related to the global tectonics of the opening of the Atlantic ocean. The rifts are filled with sediments starting in the Jurassic, and the presence of diabase intrusions and halogenic tectonics made these structures complex. The scenario of these basins features horsts, grabens, anticlines, synclines, flower structures, and dip inversions. Transcurrent faulting is considered to have reactivated local features that were developed in the rift stage. The stratigraphic scenario is divided into depositional sequences that reflect the geological evolution of the area.

## METHODOLOGY

The simplified workflow adopted is summarized in Figure 1, where the major steps follow Heilmann (2007).

The data set was offered in the form of non processed field records, therefore a complete preprocessing stage was necessary that is partially described in the sequel. To provide a first orientation regarding the main structural features present in the area, idealized geological sections are published in sites and didactic books.

The selected marine line has the following general information: date of acquisition, 1985; direction, SE-NW; length, 40 km; shot points, 1578; time sampling interval, 4 ms; shot point and receiver station spacings, 25 m; gun array and 120 hydrophone groups were placed at 8 m depth.

The preprocessing consisted of 3 main parts: (1) geometry setting; (2) zeroing bad traces; and (3) $f$-$x$ and $f$-$k$ filtering. The workflow was organized as an annotated sequence of targets in a Makefile keeping detail reference information to ensure reproducibility of the results, and to emphasize the dependence of the processing on several steps with different parameter sets. Conventional imaging was applied involving the application of the following techniques: (4) velocity analysis; (5) NMO stacking; (6) Kirchhoff time migration.

The original data was analyzed to locate noisy shot and receiver gathers, to look for dead traces, and all strongly corrupted traces were zeroed.

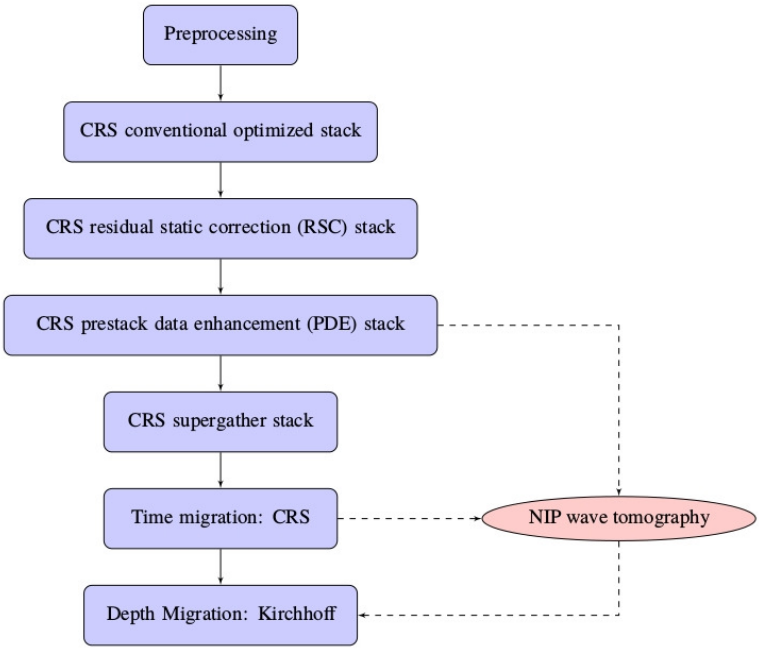


**Figure 1** – Major steps of the data processing and imaging.

A trapezoidal band-pass $f$-$x$ filter was applied, and designed with corner frequencies of 10-20-40-60 Hz. Also, a $f$-$k$ dip filter was designed and applied to suppress unwanted events outside the primaries reflection zone (Verschuur et al., 1992). The decision for adopting filter parameters was based on the visual analysis of the trace gathers, on the Fourier spectra, and on the preliminary stack results that reinforced the importance of the preprocessing stage.

Optimum linear prediction and spiking deconvolution filters were tested and applied to attenuate ocean bottom multiples, and to increase temporal resolution.

In all figure presentations an Automatic Gain Control (AGC) was adopted, although other gains were tested, and applied with a 0.5 s rectangular window width to reveal weak events.

## CRS Stack Operator

Bernabini et al. (1987) describe several functionals that have been proposed to evaluate quantitatively trace-to-trace correlation of measured data along a trajectory of a model function. In the present case, aiming at describing the hyperbolic reflection response of planar reflectors on a given CMP gather parametrized by a stacking velocity value. The most common functionals measure the likeness of the corrected gather's amplitude ($\overline{u}$) based on correlation of traces, and choices of normalization. The normalized 2D $h-x$ semblance measure, S$(t_0;\mathbf{m})$, is composed as an average given by:

$$S(t_0;\mathbf{m}) = \frac{\frac{1}{N_h}\sum_{t=t_0-\delta t}^{t=t_0+\delta t}\sum_{x_m=x_F}^{x_m=x_L}\left[\sum_{h=h_F}^{h=h_L}\overline{u}[t(x_m,h);t_0,\mathbf{m}]\right]^2}{\sum_{t=t_0-\delta t}^{t=t_0+\delta t}\sum_{x_m=x_F}^{x_m=x_L}\sum_{h=h_F}^{h=h_L}\overline{u}^2[t(x_m,h);t_0,\mathbf{m}]}, \quad (1)$$

$$(0 \leq S(t_0,\mathbf{m}) \leq 1).$$

$S(t_0;\mathbf{m})$ is function of $t_0$, given the parameter set $\mathbf{m}$. The summation goes from a first $h = h_F$ to a last $h = h_L$ half-offset with $N_h$ points; from a midpoint $x_m$ ranging from $x_F$ to $x_L$ with $N_x$ points; and in a moving time window along the hyperbolic trajectory, and specified by some $\delta t$. The measure $S(t_0;\mathbf{m})$ takes values in the interval $[0,1]$, regardless of the absolute signal amplitude, and it quantifies the uniformity of the signal polarity across the NMO corrected gather amplitude $\overline{u}[t(x,h);t_0,\mathbf{m}]$. In the NMO stack, the function S$(t_0;\mathbf{m})$ can also be interpreted as the function to be optimized, from where an optimum value of parameter stack, $\mathbf{m}$, results.

Conventional velocity analysis is performed on common-midpoint (CMP) gathers by approximating the two-way traveltime $t(h;t_0,v)$ of primary reflection arrivals from an interface by a

second order hyperbolic model of the type:

$$t(h; t_0, v) \approx \sqrt{t_0^2 + \frac{(2h)^2}{v^2}}; \qquad (2)$$

to be considered as part of the Equation (1) for 1D to search for the attribute $\mathbf{m} = v$, where $h$ stands for the half source-receiver offset, $t_0$ for the normal two-way traveltime at $h = 0$, and $v = v_{\text{NMO}}$ denotes the normal moveout velocity. In the section Results we show the NMO conventional stack based on a shown velocity model, but still limited for interpretational use, and it is to be compared with other similar figures.

The above law (2) is exact for a single horizontal reflector with homogeneous overburden, and for the next level of complexity one can consider an ideal medium composed of multiple homogeneous, isotropic, layers with horizontal interfaces, an the above law still constitutes a reasonably accurate approximation, as described by Ursin (1982). The criterion for expressing quantitatively the degree of fitting between the model controlled by the $v_{\text{NMO}}$ velocity value and the data usually involves a coherence measure such as $S(t_0; \mathbf{m})$. A typical algorithm for velocity analysis in the $h-t$ domain calculates at each point $t_0$ the velocity spectrum which consists of a coherence value for every $v_{\text{NMO}}$ within a given search range. In practice, often a simple 1D approximation is used to calculate the interval velocities of the medium from the previously determined $v_{\text{NMO}}$ velocity distribution, where the $v_{\text{NMO}}$ velocity is considered to approximate the root-mean-square (RMS) velocity $v_{\text{RMS}}$, as described by Al-Chalabi (1992). A figure is presented in section Results for a velocity model obtained by semblance velocity analysis.

Turning to a more realistic 3D subsurface geological model, one can be constructed with an inhomogeneous velocity distribution that can be smooth, or with discontinuities represented by curved interfaces. Under such geometrical conditions, limitations of the NMO correction physically emerges. But, the CRS stack concept can take this more complex reflector geometry explicitly into account, by extending the velocity analysis from a time-offset to a time-offset-midpoint domain. Following Mann (2002), the CRS stack operator is formulated for 2D and 3D models formed by homogeneous and isotropic layers limited by arbitrarily curved interfaces for the two-way traveltime of primary reflections based on paraxial ray theory. Considering the 2D seismic with a flat observation surface, the time operator is given by:

$$t_{\text{hyp}}(x_m, h; \mathbf{m}) \approx \sqrt{\left[t_0 + \frac{2\sin\beta_0 (x_m - x_0)}{v_0}\right]^2 + \frac{2t_0 \cos^2\beta_0}{v_0}\left[\frac{(x_m - x_0)^2}{R_{\text{N}}} + \frac{h^2}{R_{\text{NIP}}}\right]}. \qquad (3)$$

This time function is to be considered as part of Equation (1), and adapted to the specific search for the attributes $\mathbf{m} = (\beta_0, R_{\text{NIP}}, R_{\text{N}})$ related to the central ray. The stack reference point is named $P_0(x_0, t_0)$, and it is assumed that the velocity $v_0$ is known, related to the upper layer, and around the observation point $x_0$. The independent variables $x_m$ and $h$ are the midpoint coordinate and the half-offset, respectively.

The CRS stack operator (3) is constructed not to be explicitly dependent on a macro-velocity model in the $x - t$ domain, and it is employed in an automatic data-driven parameter search based on the semblance. This operator is parametrized using two hypothetical eigenwaves generating the Normal-Incidence-Point (NIP) and the Normal (N) waves. The NIP wave is associated with an exploding diffractor (or point source) at the NIP point of the zero-offset ray, and reaches the surface at $x_0$ with radius $R_{\text{NIP}}$. The N-wave is associated with the exploding reflector concept around the NIP location, and generates the Normal wave which reaches the surface at $x_0$ with radius $R_{\text{N}}$. The parameter $\beta_0$ corresponds to the common emergence angle of the both wavefronts at the observation point $x_0$.

In the context of paraxial ray theory, a central ray is considered with normal incidence on the reflector at the NIP point. Furthermore, only primary events are taken into account. The central ray satisfies Snell's law across the interfaces, and the wavefront curvatures of the NIP and N waves change according to the refraction and transmission laws of curvature, as described by Hubral & Krey (1980).

In practice, the algorithm requires CDP numbers, the source coordinates $x_S$, and the receiver coordinates $x_G$. Their relationship to the $x_m$ and $h$ coordinates are given by $x_m = (x_G + x_S)/2$ and $h = (x_G - x_S)/2$. The semblance parameter analysis is performed along the stacking operator (3) spanned by the coordinates $h$ and $x_m$ according to Equation (1). The parameter vector $\mathbf{m}$ takes the elements $\mathbf{m} = (R_{\text{NIP}}, R_{\text{N}}, \beta_0; v_0)$, where the elements (with $v_0$ fixed) are searched for as an optimization problem with the semblance (1) as the object function, and the CRS operator (3) as the forward model. The multiparametric search is classified as a nonlinear problem; therefore, the optimization strategy would need a starting point, $\mathbf{m}^{(\text{ini})}$, in the parameter space, and parameter sensitivity derivatives,

or a controlled random search without derivatives. Müeller et al. (1998) and Mann (2002) describe strategies for the parameter search basically performed in four steps.

Mann (2002) described the problem related to conflicting dips in the stack sections, analyzed the dependence of $v_{\text{NMO}}$ on $\beta_0$, and proposed a solution by detecting multiple values of $\beta_0$ for each contributing event, by adapting the original search strategy of Müeller et al. (1998). Soleimani et al. (2009) also addresses the conflicting dip problem by proposing a strategy that considers a multitude of different values of $\beta_0$ for each ZO sample, with the forward model (3) under the condition $R_{\text{N}} = R_{\text{NIP}}$ to improve the continuity of reflection events and diffraction events, in a process named common-diffraction-surface stack.

Several figures in the section Results show the main products of the full stack process, as for $\mathbf{m} = (R_{\text{NIP}}, R_{\text{N}}$ and $\beta_0)$, where we call attention to the section textures and the similarity of patterns.

### CRS Mapping Migration

The first appearance of this method was in Mann et al. (2000), where it considers that the CRS attributes can approximate the (hypothetical) diffraction associated with a reflection event and, therefore, a Kirchhoff-type migration operator.

The apex of the ZO diffraction response provides an approximation of the image location for time migration, and the principle is that $\partial t_{\text{hyp}}(x_m, h = 0)/\partial x_m = 0$ for the ZO plane $h = 0$, due to the symmetry considerations, to yield the apex location given by:

$$x_{\text{apex}} = x_0 - \frac{R_{\text{NIP}} t_0 v_0 \sin\beta_0}{2R_{\text{NIP}}\sin^2\beta_0 + t_0 v_0 \cos^2\beta_0}\,; \qquad (4)$$

$$t_{\text{apex}} = \sqrt{\frac{{t_0}^3 v_0 \cos^2\beta_0}{2R_{\text{NIP}}\sin^2\beta_0 + t_0 v_0 \cos^2\beta_0}}\,. \qquad (5)$$

This approximate ZO diffraction response can be parametrized in terms of the apex location ($x_{\text{apex}}$, $t_{\text{apex}}$) instead of the ZO location ($x_0$,$t_0$):

$$t_{\text{hyp}}(x) = \sqrt{t_{\text{apex}}^2 + \frac{4(x - x_{\text{apex}})^2}{v_c^2}}, \qquad (6)$$

where

$$v_{\text{c}} = \sqrt{\frac{2v_0^2 R_{\text{NIP}}}{2R_{\text{NIP}}\sin^2\beta_0 + t_0 v_0 \cos^2\beta_0}}\,. \qquad (7)$$

This allows a summation along the approximate diffraction response, with the result assigned to its apex. Even more convenient, the already available stack value computed along the CRS operator can be mapped to the apex ($x_{\text{apex}}$, $t_{\text{apex}}$).

### Residual Static Correction

Aiming at increasing resolution, the Residual Static Correction (RSC) strategy has been applied under the concept of source-receiver displacements, and in terms of looking for better correlation between the ZO trace and the correspondent family traces under small shifts. The result is only shown by its coherence map in the figures shown in the sequel, where we compare with the resolution of the other processes.

Koglin et al. (2006) describe the CRS-based RSC as an iterative process similar to the super-trace cross-correlation method as presented by Ronen & Claerbout (1985). In this approach, the cross-correlations are performed with the CRS supergathers consisting of all moveout corrected prestack traces within the spatial stacking aperture, instead of being confined to individual CMP, common-shot, or common-receiver gathers. Due to the spatial extent of the employed stacking operator, a supergather contains several neighboring CMP gathers. For each considered supergather centered around a particular ZO location, the moveout correction will, in general, be different. Since each prestack trace is included in several different supergathers, it contributes to more cross-correlations than in methods using only individual gathers. The cross-correlations of the stack pilot trace and the moveout corrected prestack traces are summed up for each shot and receiver location. This summation is performed for all supergathers contained in the specified target zone. The searched for residual time shifts are then expected to be associated with the locations of the maxima in the cross-correlation stacks, and they are used to correct the prestack traces. The stack result after RSC shows an improvement in resolution, and we present in the Results.

### Prestack Data Enhancement

As a next step aiming at increasing resolution (Bardan, 2005), the concept of Prestack Data Enhancement (PDE) by interpolating new CDPs based on the CRS stack operator and data-driven attributes, as described by Baykulov & Gajewski (2007), has been integrated into the processing workflow, and is shown in Figure 1.

The CRS-based interpolation constructs supergathers at prescribed positions $x_m$, it results in better visual zero-offset sections, and in a bigger spatial Nyquist frequency for aliasing spectral analysis. By increasing the number of trace the signal/noise ratio increases following the rule $\sqrt{N}$, as described by Sengbush (1983), and solving the aliasing problem, as described by Bardan (2005).

Using the CRS attributes $\beta_0$ and $R_{\text{NIP}}$, the corresponding time $t_{\text{par}}$ obtained from the $t_0$ is given by:

$$t^2_{\text{par}}(x_m,h) = \left(-\frac{h^2\cos^2\beta_0}{v_0 R_{\text{NIP}}} + \sqrt{\left(\frac{h^2\cos^2\beta_0}{v_0 R_{\text{NIP}}}\right)^2 + t^2_{\text{hyp}}(x_m,h)} + \frac{2\sin\beta_0}{v_0}x_m\right)^2 + \frac{2\cos^2\beta_0}{v_0}\left(-\frac{h^2\cos^2\beta_0}{v_0 R_{\text{NIP}}} + \sqrt{\left(\frac{h^2\cos^2\beta_0}{v_0 R_{\text{NIP}}}\right)^2 + t^2_{\text{hyp}}(x_m,h)}\right) \times \left(\frac{x_m^2}{R_{\text{N}}} + \frac{h^2}{R_{\text{NIP}}}\right). \quad (8)$$

Depending on the quality of the data and on the acquisition geometry, the lateral windows for stacking can be optimized in the directions $x_m$ and $h$. In our examples the window sizes were the same as chosen for the CRS stack. The stack results after PDE showed more improvement in resolution than the RSC, where the comparative measure is based on the semblance scale values, and on the visual continuity of events, as shown in the figures of the section Results.

### Fresnel Volume

The Fresnel Volume (FV) concept (Kravtsov & Orlov, 1990) relates to the region between the point source and the receiver, where the wave field is affected by the geological structure around a central ray. Sheriff & Geldart (1995) and Cerveny (2001) describe the geometry of Fresnel Zones (FZ), where the condition of zero-offset is emphasized, considering a monochromatic wave. The main contribution of the reflected energy comes from the First Fresnel Zone (FFZ) that has radius

$$R_1 = \sqrt{\frac{1}{2}\lambda z_0} = \frac{1}{2}v_{\text{A}}\sqrt{\tau/f},$$

where $z_0$ is the depth of the reflector, $\lambda$ is the wavelength, $v_{\text{A}}$ is the average velocity, $\tau$ is the traveltime reflector-receiver, ($\tau = t/2$), and $f$ the frequency. The Fresnel Volume and Zone are closely related, and Hubral (1999) describes the concept of the Projected First Fresnel Zone (PFFZ) to the surface to represent an optimum aperture for stack.

Mann (2002) defines the PFFZ around an arbitrarily chosen central ray as the difference between the diffraction, $t_D(\mathbf{x})$, and reflection, $t_R(\mathbf{x})$, traveltimes from the source down to each point on the reflector and up to the receiver, and that satisfies:

$$|t_D(\mathbf{x}) - t_R(\mathbf{x})| \leq \frac{1}{2f}. \quad (9)$$

Using the parabolic approximation for the CRS operator, the borders of the PFFZ are given by

$$|t_D(x_m - x_0, h) - t_R(x_m - x_0, h)| = \frac{1}{2f},$$

with $R_{\text{N}} := R_{\text{NIP}}$ for $t_D$, and a simple solution is obtained:

$$\frac{1}{2f} = \left|\frac{\cos^2(\beta_0)(x - x_m)^2}{v_0}\left(\frac{1}{R_{\text{N}}} - \frac{1}{R_{\text{NIP}}}\right)\right|. \quad (10)$$

This expression is offset independent, and solving for $(x_m - x_0)$ yields an approximation for the PFFZ for the ZO configuration, as given by:

$$\frac{W_{\text{F}}}{2} = |x_m - x| = \frac{1}{\cos(\beta_0)}\sqrt{\frac{v_0}{2f\left|\frac{1}{R_{\text{N}}} - \frac{1}{R_{\text{NIP}}}\right|}}. \quad (11)$$

This volume measure is illustrated in the section Results.

### Conflicting Dips

For the conflicting event issue, it is expected that a $t - x$ stack and poorly migrated sections to display crossing events characterized by different dips. The section should show continuity of the main and secondary events at the crossing, and not an empty gap or discontinuities that are marked in the semblance domain.

The main event is defined as related to the global coherence maxima along a window in the $t_0 - v_{\text{rms}}$ map, and the crossing events are taken as a secondary local maxima located within a minimum distance from the main event.

Mann (2002) handles this case by determining additional coherence maxima in the linear ZO stack, and presents a strategy to consider different values for $R_{\text{N}}^{(\text{i})}$ and $\beta_0^{(\text{i})}$, $(i = 1, 2, \ldots, n)$, where $n$ is the number of the considered searches for event crossings for each ZO sample, and the search for $R_{\text{NIP}}^{(\text{i})}$ is performed in the prestack common-shot and common-receiver data.

On the other hand, Soleimani et al. (2009) address the conflicting dip issue by considering a stack operator called CDS (common diffraction surface) where $R_{\text{NIP}} = R_{\text{N}}$ are substituted by $R_{\text{CDS}}$ in Equation (3), and it is written in the form:

$$t_{\text{hyp}}(x_m, h; \mathbf{m}) = \sqrt{\left[t_0 + \frac{2\sin\beta_0}{v_0}(x_m - x_0)\right]^2 + \frac{2t_0\cos^2\beta_0}{v_0 R_{\text{CDS}}}\left[(x_m - x_0)^2 + h^2\right]}; \quad (12)$$

where $R_{\text{CDS}}$ is searched for each $\beta_0$, with the latter being defined on a user given grid.

The CRS sections here presented were obtained considering up to three conflicting dip directions. Sometimes they are well resolved, and in some cases the crossing events show a discontinuation, what can be analyzed in the stack figures of section Results.

### NIP Wave Tomography

The inversion of seismic reflection data is a typical nonlinear, multiparametric, mixed-determined problem. Therefore, the classical solution is composed of at least two main parts: curve matching and solution smoothness, as described by Tarantola (2005).

Duveneck (2004) gives the details of the NIP wave tomography as a technique to obtain a depth velocity distribution based on nonlinear curve fitting between data and model for a number of $n_{\text{data}}$ observation points representing the NIP wave, as illustrated in Figure 2. For the 2D case, the inversion input data is defined by:

$$d_i = (\tau_0, M, p, x_0)_i, \qquad (i = 1, 2, \ldots, n_{\text{data}}), \quad (13)$$

from picked points on the CRS stack section, where $\tau_0 = \frac{t_0}{2}$ is the one-way traveltime, and $x_0 = \xi_0$ is the ray emergence point at the surface. For the curve matching process, the model quantities $d_i$ are calculated by dynamic ray tracing.

The quantity

$$M = \frac{\partial^2 t(x_1, x_2)}{\partial x_1 \partial x_2}, \quad (x_1 = x = \xi, x_2 = z),$$

is the second order partial derivative of the traveltime with respect to the ray centered space coordinates $(x_1, x_2)$, also expressed by $M_i = (v_0 R)_i^{-1}$, with $v_0$ known, and $R_i$ points taken from the CRS $R_{\text{NIP}}$ section. The quantity $p = \frac{\partial t}{\partial x_1}$ is the partial derivative of the traveltime with respect to the ray centered space coordinate $(x_1)$, and also related to $p_i = \frac{\cos\beta_0}{v_0}$, with $\beta_0$ taken from the CRS $\beta_0$ section.

The aim of the inversion process is to find a subsurface velocity model, based on the observed data, and defined by the following parameters:

$$\begin{aligned} m_i^{(\text{NIP})} &= (x, z, \theta_x)_i \quad (i = 1, 2, \ldots, n_{\text{data}}) \\ m_{jk}^{(\text{v})} &= v_{jk} \qquad\qquad (j = 1, 2, \ldots, n_x; \\ &\qquad\qquad\quad k = 1, 2, \ldots, n_z); \end{aligned} \quad (14)$$

where $(x, z)$ are the spatial coordinates of the model grid points with the spline velocity values $v_{jk}$, and $\theta_x$ the vertical angle of the unit vector normal to the reflector.

The strategy is that the deviations $(\Delta\mathbf{d})$ between the input $(\mathbf{d}^{\text{obs}})$ and model $(\mathbf{d}^{\text{pre}})$ points be minimized in the least-squares sense, and the fitting to only depend on the velocity model changes as described by a fourth order B-spline in the form:

$$v(x, z) = \sum_{j=1}^{n_x}\sum_{k=1}^{n_z} v_{jk}\beta_j(x)\beta_k(-z), \quad (15)$$

The object function of minimization is composed by a measure of fitness between observed and model data, and by the solution smoothness, and it is written as:

$$S(\mathbf{m}) = \frac{1}{2}\Delta\mathbf{d}^{\mathsf{T}}(\mathbf{m})\mathbf{C}_{\text{D}}^{-1}\Delta\mathbf{d}(\mathbf{m}) + \frac{1}{2}\varepsilon\mathbf{m}^{(v)\mathsf{T}}\mathbf{D}\mathbf{m}^{(v)}. \quad (16)$$

The fitting process can be constructed via Taylor series, that is applied to locally linearize the model function, $f(\boldsymbol{m})$, in the neighborhood of $\mathbf{m}$ in the form:

$$f(\mathbf{m} + \Delta\mathbf{m}) \approx f(\mathbf{m}) + \mathbf{F}\Delta\mathbf{m};$$

where $\mathbf{F}$ is the derivative matrix,

$$F_{ij} = \frac{\partial f_i}{\partial m_j} = \frac{\partial(\tau_0, M, \beta_0, \xi)}{\partial(x, z, \theta, v)},$$

calculated at the actual point $\mathbf{m}$, and $\Delta\mathbf{d}(\mathbf{m}) = \mathbf{d}^{(\text{obs})} - \mathbf{f}(\mathbf{m})^{(\text{pre})}$. The iterative solution update has the form:

$$\mathbf{m}^{(k+1)} = \mathbf{m}^{(k)} + \gamma\Delta\mathbf{m}^{(k)},$$

where the $\gamma$ factor controls the step size $\Delta\mathbf{m}$ of the $k$ iteration.

The smoothness matrix $\mathbf{D}$ is positive definite, and $\varepsilon$ weights the contributions between the fit and smoothness terms. $\mathbf{C}_{\text{D}}$ is the data symmetric diagonal covariance matrix for non correlated errors. Every point of Equation (16) has four types of data as in Equation (13): traveltime, second order traveltime derivative, first-order traveltime derivative, and spatial coordinates. Due to the difference in scale quantities, it is necessary to choose adequate scale factors to $\sigma_\tau, \sigma_M, \sigma_p$ and $\sigma_\xi$. After the problem construction, the parameter vector is given by:

$$\mathbf{m} = \left(\mathbf{m}^{(\text{NIP})}\ \mathbf{m}^{(v)}\right)^{\mathsf{T}}.$$

Regularization is a central issue in NIP wave tomography, as in all geophysical inverse problems (Gupta, 2011),

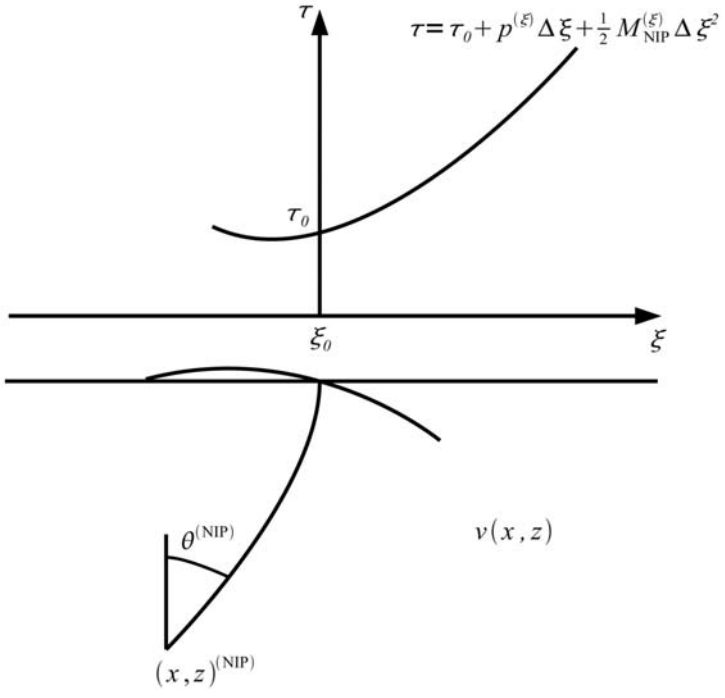


**Figure 2** – Geometrical parameters of the tomography 2D model with respect to the NIP position.

and a more physically consistent concept is that the second order derivative operator, $\mathbf{m}^{\mathsf{T}}\mathbf{D}\mathbf{m}$, should have minimum length, since second derivatives represent a measure of curvature, penalizing the roughness of the velocity model. The solution is therefore for smoothness, a condition necessary to assure the validity of the paraxial ray theory. For the 2D $(x, z)$ case, the regularization term $(\frac{1}{2}\varepsilon\mathbf{m}^{(v)\mathsf{T}}\mathbf{D}\mathbf{m}^{(v)})$ is resumed to the form:

$$\frac{1}{2}\varepsilon\mathbf{m}^{(v)\mathsf{T}}\mathbf{D}\mathbf{m}^{(v)} = \int_z\int_x\left[\varepsilon_{xx}(x,z)\left(\frac{\partial^2 v(x,z)}{\partial x^2}\right)^2 + \varepsilon_{zz}(x,z)\left(\frac{\partial^2 v(x,z)}{\partial z^2}\right)^2 + \varepsilon v^2(x,z)\right]dxdz; \qquad (17)$$

where the integral expresses the weighted averaging process over the roughness measure (second derivatives), and where $v(x, z)$ is given by Equation (15). This measure is useful around the borders of the model where information is scarce to constrain the B-splines coefficients.

For the inversion process, it is necessary to calculate Fréchet derivatives, $F_{ij}$, for the modeled quantities $d_i = (\tau_0, M, p, x_0)_i$ with respect to the NIP model parameters $(x, z, \theta_x)^{\mathrm{NIP}}$ and to the velocity model parameters $v_{jk}$.

The forward modeling in the 2D case is performed with dynamic ray tracing in ray-centered coordinates ray by perturbation theory to calculate the model updates $\Delta\mathbf{m} = (\Delta\mathbf{x}, \Delta\mathbf{z}, \Delta\theta_{\mathbf{x}}, \Delta\mathbf{v})$, from the data deviations $\Delta\mathbf{d} = (\Delta\tau_{\mathbf{0}}, \Delta\mathbf{M}, \Delta\mathbf{p}, \Delta\mathbf{x_0})$.

Results of the inversion process, and follow up applications are shown in the sequel.

## RESULTS

Figure 3 shows the NMO conventional stack-based on the velocity model of Figure 4 obtained by semblance velocity analysis, and it still is limited for interpretational use.

Figure 5 shows the selected stack result, where lines can be drawn to separate the section in two event types: an upper part with subhorizontal reflector patterns; and a lower part with subvertical diffraction patterns. It is clear the complex seismic-geological structure of the section, but that it is a 2D seismic, where lateral structures can participate as crossing events. Figure 5 is followed by the $R_{\mathrm{NIP}}$, $R_{\mathrm{N}}$ and $\beta_0$ attributes shown in Figures 6, 7 and 8, that exhibit a consistent behavior in the figures for $R_{\mathrm{N}}$ and $\beta_0$, that resemble the structured stack of Figure 5 and the coherence in Figure 19. Also, the consistency in Figure 6 of the $R_{\mathrm{NIP}}$ attribute that shows a systematic increase with time.

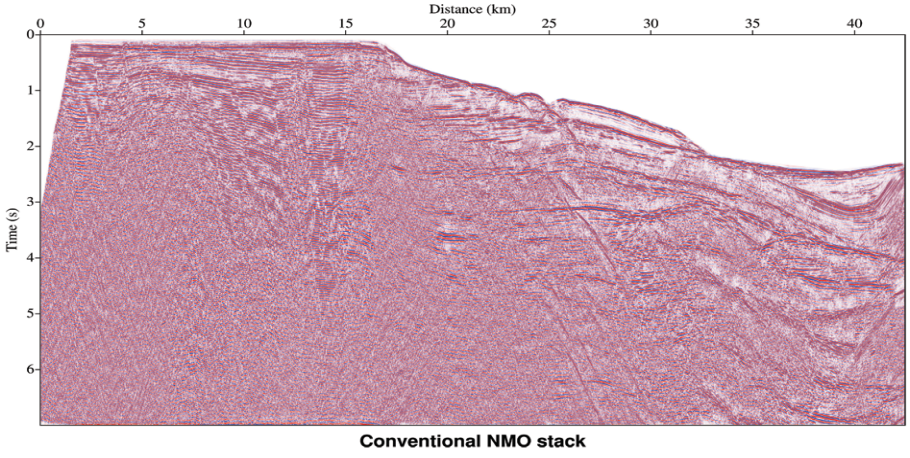


**Figure 3** – Conventional NMO stack. Compared with the CRS Fresnel supergather stack of Figure 5. Notice the multiples characterized by the shape and time with respect to the sea floor primary event.

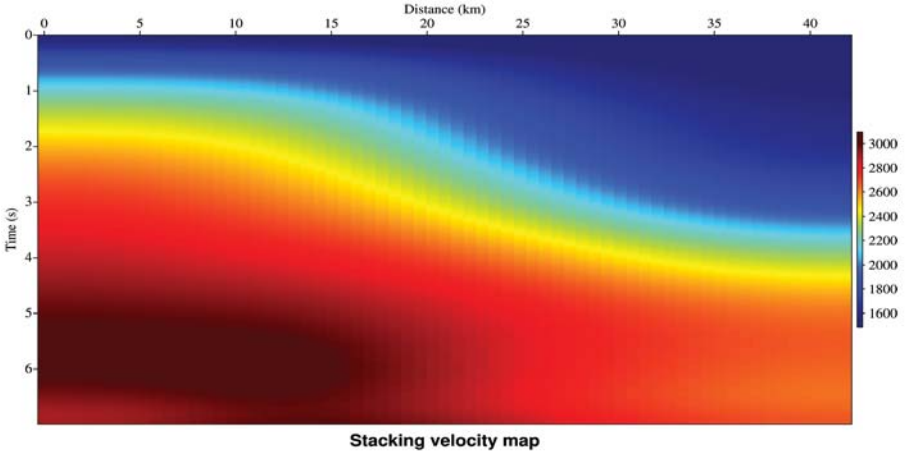


**Figure 4** – Smooth semblance velocity map for the conventional NMO stack (Fig. 3), and for the poststack Kirchhoff time migration (Fig. 11).

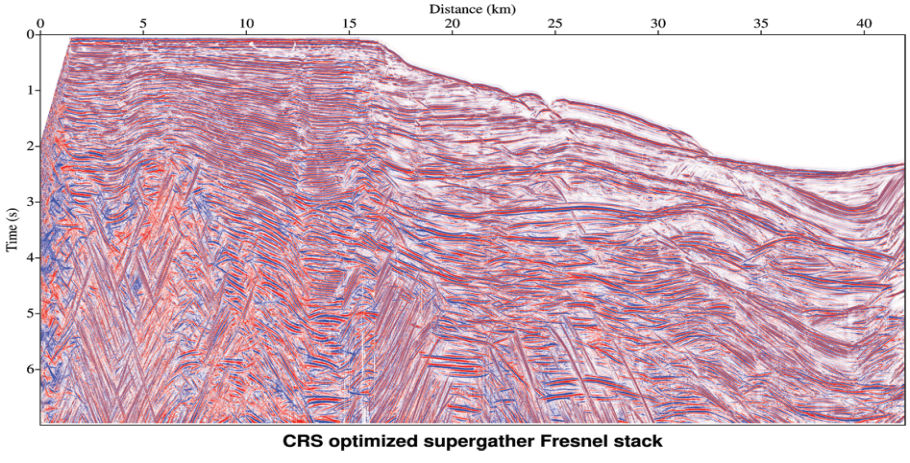


**Figure 5** – CRS optimized supergather stack with the ZO aperture restricted to the attribute-based First Projected Fresnel Zone. Compare with the conventional NMO stack of Figure 3, and with the CRS migration of Figure 10.

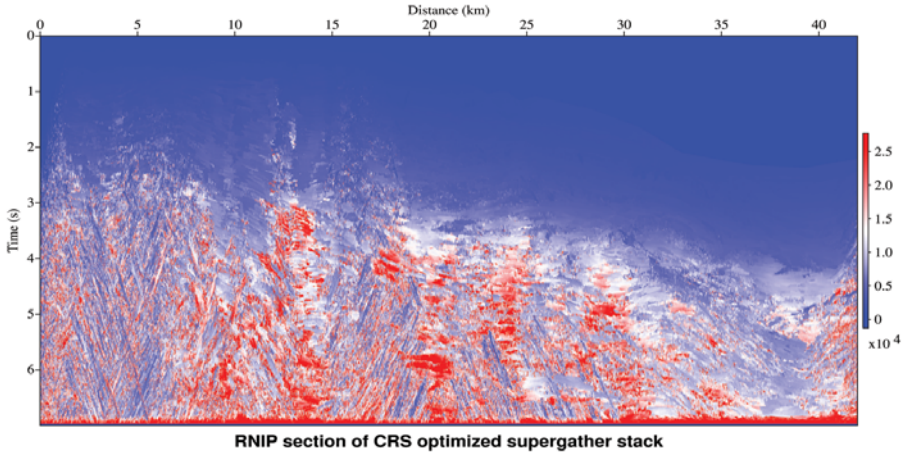


**Figure 6** – Radius $R_{\text{NIP}}$ section of the CRS Fresnel supergather stack.

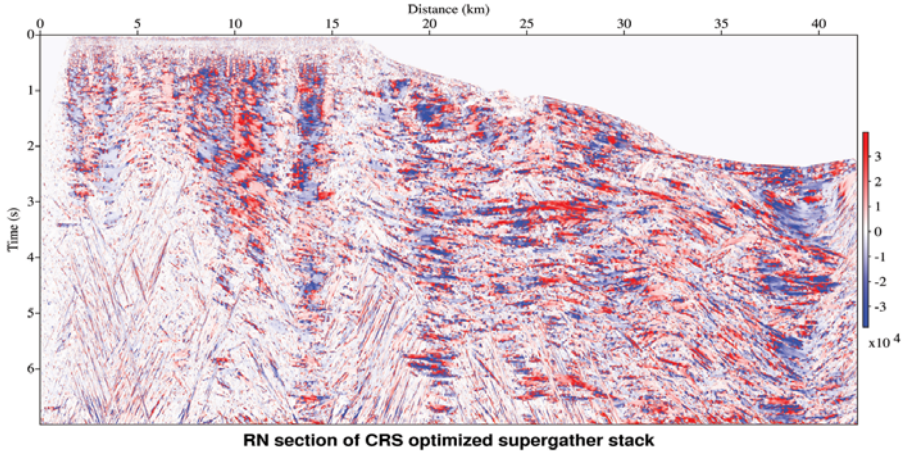


**Figure 7** – Radius $R_{\text{N}}$ section of the CRS Fresnel supergather stack.

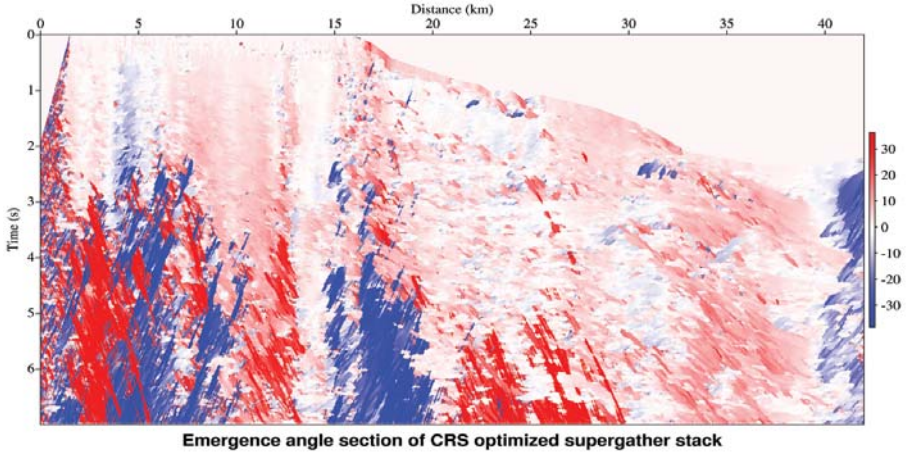


**Figure 8** – Angle $\beta_0$ section of the CRS Fresnel supergather stack.

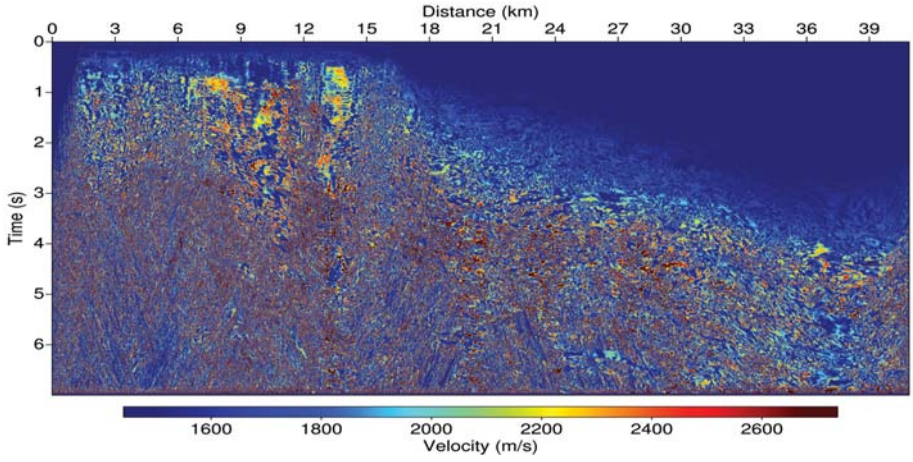


**Figure 9** – Velocity model $v_c$ without smoothing obtained directly from formula (7).

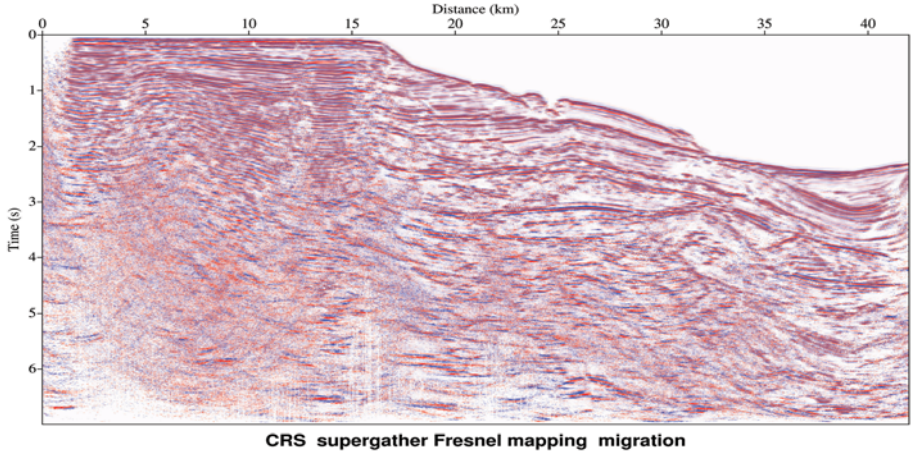


**Figure 10** – CRS supergather time migration related to Figure 5, where the aperture was restricted to the attribute-based First Projected Fresnel Zone. Compare with the Kirchhoff time migration of Figure 11.

Figure 9 shows the result for the velocity distribution $v_c$ of the CRS migration mapping, where the palette indicates a consistent variation from 1500 to 3000 m/s, but with a noisy aspect, that can be related in part to the parameter correlations.

Figure 10 shows the CRS mapping migration, that can be compared mainly with the Kirchhoff time migration of Figure 11. Figure 10 shows the evolution of the process, where some structures can be interpreted, but Figure 11 shows artifacts to be resolved for.

The time velocity distribution of Figure 4 was transformed into a velocity depth distribution using the Dix transform that is shown in Figure 12. The correspondent depth migrated section is shown in Figure 13, that was obtained by controlling the initial migration aperture from 100 m to 1000 m in the experiments, and a 300 m aperture was chosen for presentation. This figure shows horizontal structural lines in the lower part of the section.

To complement the results, it is important to analyze the Fresnel Zone aperture as illustrated in Figure 14, that shows how the aperture measure varies along the line and in time.

Figure 15 shows the obtained NIP wave tomography velocity model, and Figure 16 the correspondent Kirchhoff depth migration using the aperture shown in Figure 14 (Silva, 2012).

Special attention goes to the coherence sections of Figures 17, 18 and 19 that we used to measure the development of the processing using as reference the maximum values shown on the color scales. The CRS supergather Fresnel optimized stack were figures selected for discussions based on the quality improvement. Other figures presented are for completeness and comparison, and we distributed them according to the processing

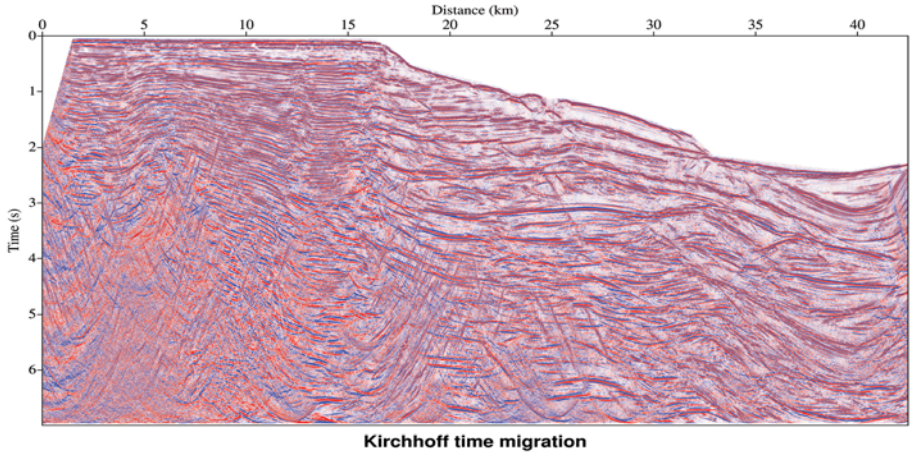


**Figure 11** – Poststack Kirchhoff vertical time migration obtained with the velocity model of Figure 4. Compare with the CRS migration of Figure 10.

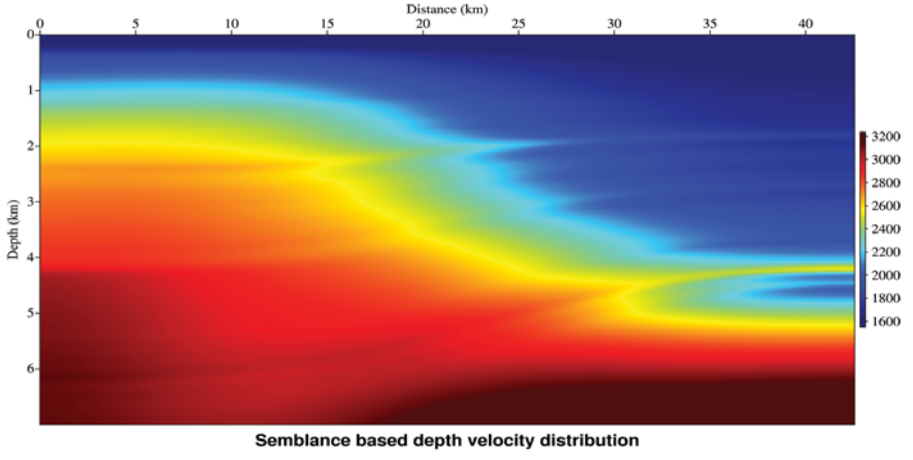


**Figure 12** – Semblance based depth velocity distribution for the poststack Kirchhoff depth migration (Fig. 13) obtained from time-to-depth velocity transformation of Figure 4.

order. Figure 19 is used to identify locations with low coherence values considered not to be associated with significant attributes ($R_{\text{NIP}}$, $R_{\text{N}}$, $\beta_0$). It is considered that subsurface structures be represented by clear patterns, and the better images associated with stronger patterns of continuity and higher values of coherence.

## DISCUSSIONS

In this part we call attention to the interpretation of the stack and migration sections, where tracing lines may need some geological-structural *a priori* information, and it is an interactive, non-unique, interpretation process. Only an interactive forward modeling, inversion and appraisal could serve as a measure estimation of the interpretational lines. Since the final aim of the full processing is to obtain good migrated sections, the stack of Figure 20, and the migration of Figure 21 are presented with the superimposed interpretation lines, that serve to indicate the stability of the processing steps, and their potential use to underline geological structures.

The stacks (Figs. 3 and 5) are compared to the time migration (Fig. 10), and they clearly show the water layer bottom followed by the response of the basin sediments with several reflection events with similar structural attitude. The basement is not easily visualized (interpreted as the last red lines in the bottom of the sections), and the stack sections display the presence of free surface and internal multiples, and diffraction events. The CRS migration section is free from the strong diffraction patterns, and show the collapsed diffraction points.

The kinematic wavefield attributes $R_{\text{NIP}}$, $R_{\text{N}}$, and $\beta_0$, (Figs. 6, 7 and 8) show their proper geometrical forms and trends limited by the color scales. From the point of view of the optimization stack

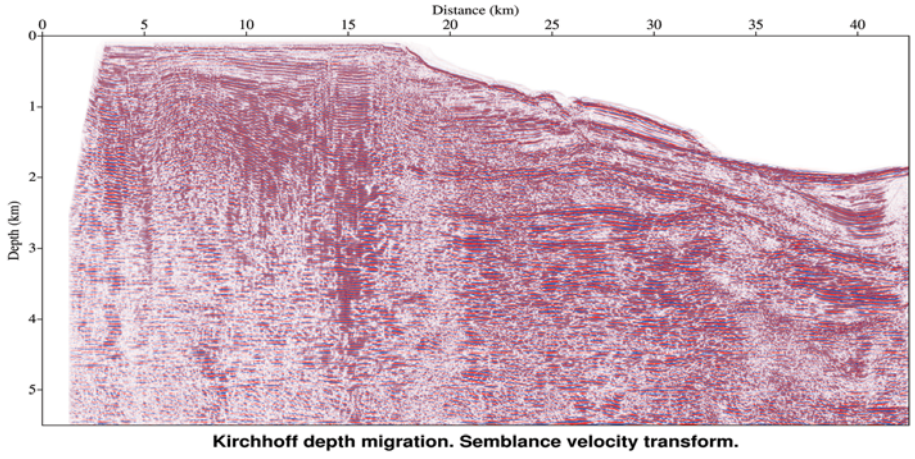


**Figure 13** – Poststack Kirchhoff depth migration obtained with the semblance velocity model transformed to depth and presented in Figure 12.

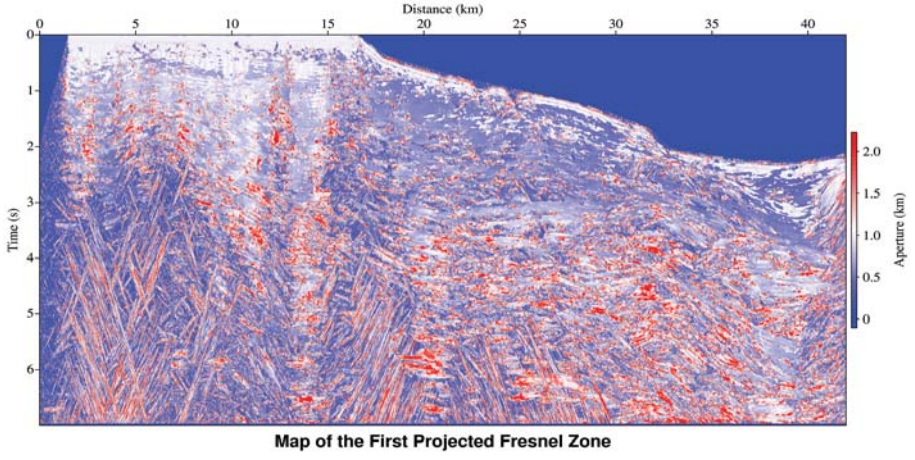


**Figure 14** – CRS Fresnel aperture as calculated by formula (11). Notice that it resembles the coherence sections (Figs. 17, 18 and 19).

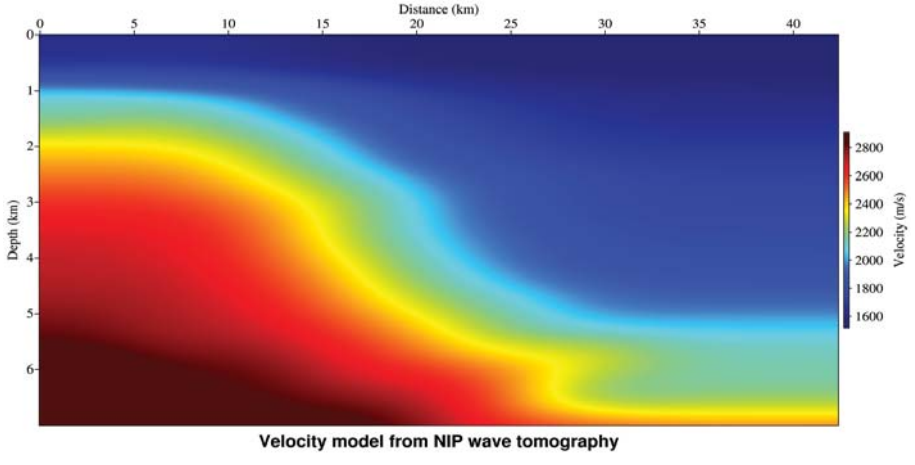


**Figure 15** – Depth velocity model obtained from NIP wave tomography inversion used for the migration result shown in Figure 16.

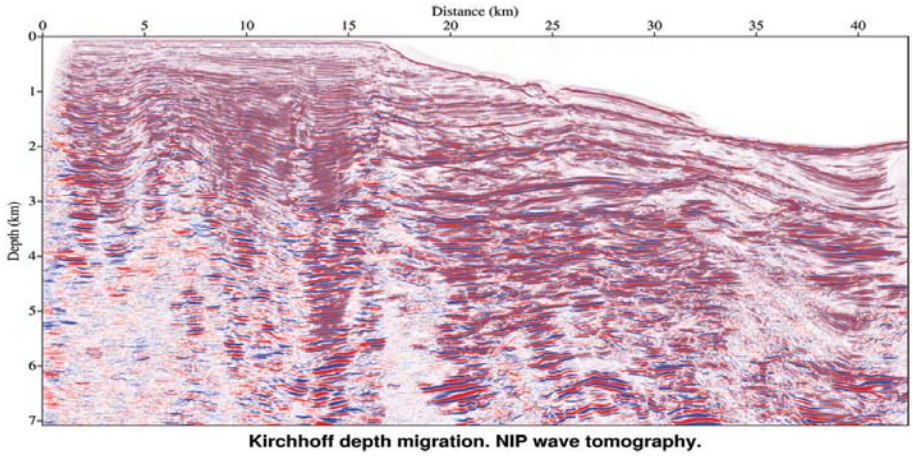


**Figure 16** – Kirchhoff depth migration obtained with the velocity model from NIP wave tomography of Figure 15.

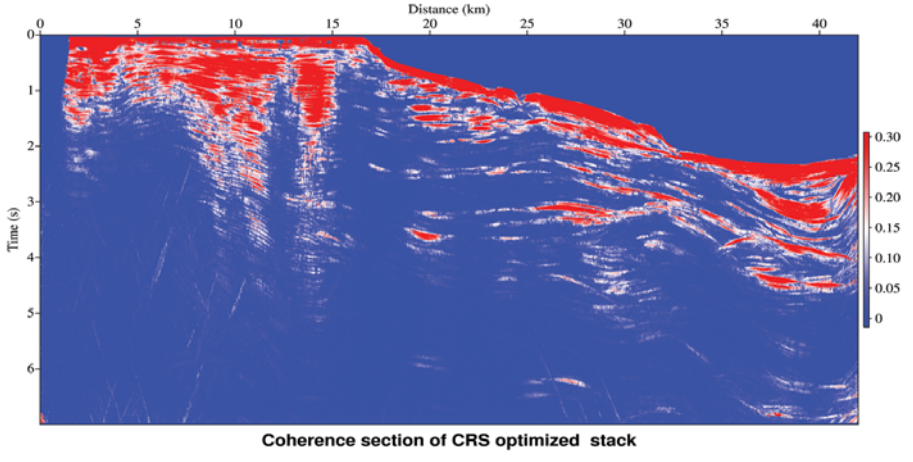


**Figure 17** – Coherence section of the CRS Fresnel conventional stack showing a maximum value around $S = 0.30$.

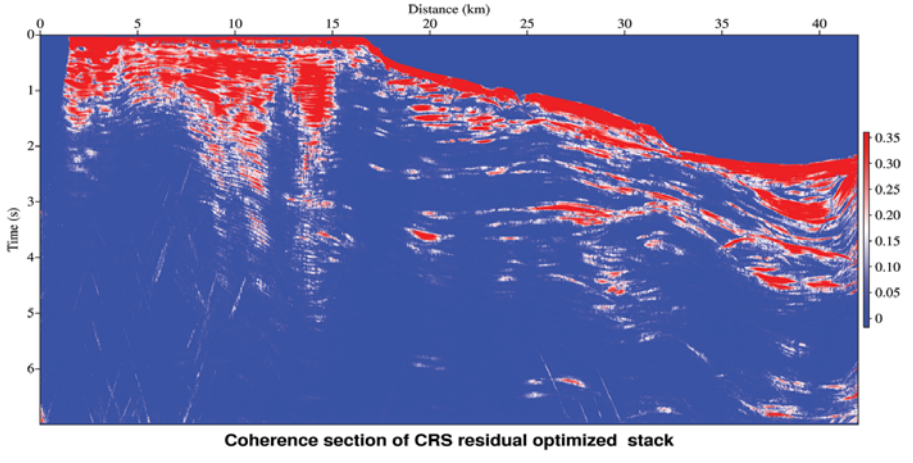


**Figure 18** – Coherence section of the CRS Fresnel residual static correction. Notice the different color scale with a maximum value around $S = 0.35$ indicating a small increase with respect to Figure 17.

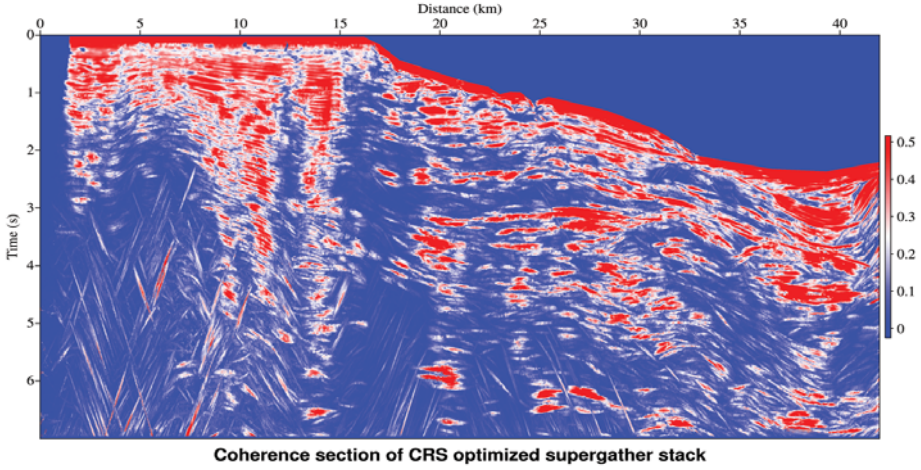


**Figure 19** – Coherence section of the CRS Fresnel optimized supergather stack (Fig. 5), where the color scale reaches a maximum value around $S = 0.51$ indicating a larger increase with respect to Figure 17.

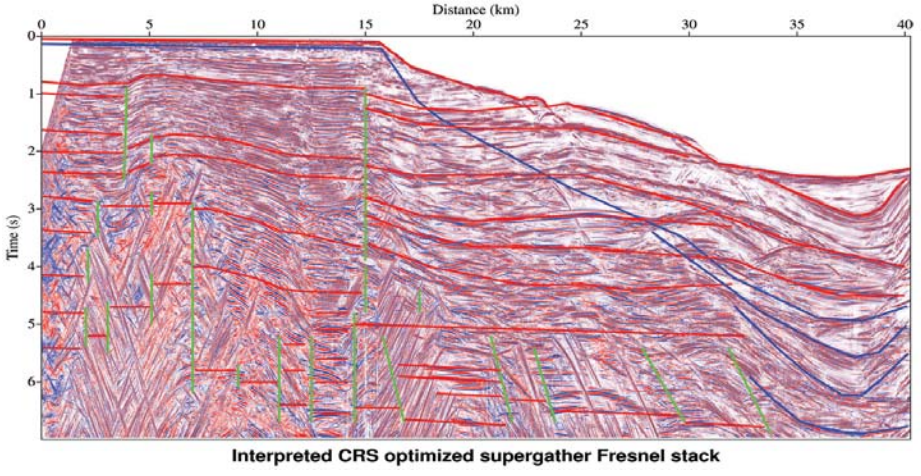


**Figure 20** – The color lines were based on the stack and migration sections, and meant to separate the different seismic event patterns.

algorithm, the procedure should first point to a global maximum of the coherence semblance function representing the most predominant events. Secondary semblance maxima can be presented as other attribute sections, for the correspondent and significant crossing events with conflicting dips.

For further analysis of Figures 20 and 21, it is important that the maps have scale exaggeration, and *a priori* geological information. From proper screen display, and details of the used geological sections for the area, we can trace discontinuities, anticlines and faults. Also, the lower-left part of the section of Figure 21 would need more attention for structures to be better recognized under the stack due to the strong diffraction events, and the lower-right part due to the strong multiple events.

The original lines in Figure 20 were transferred to Figure 21 to verify relative changes on positions of the reflection events. Comparing these figures in details, they show that there is almost no shift between the interpretation lines for the horizontal events, but consistent shift for the dipping events. From Figure 21 one can see that the most prominent diffraction feature on the left-bottom side collapsed, and some reflection events now appear. From this observation, we can say that the stack operator maps well into the time migration domain.

The main points for analysis and interpretation are related to the basement structure, and to the superimposed sedimentary sequence based on the lateral continuity of the reflection field, on the resolution, and to the texture and frequency content in the block divisions of the main stack and migration sections, that can be used to interpret the geological contacts and units. As a first conclusion, a diffraction-based stack should be applied to help further the geological integration of these results.

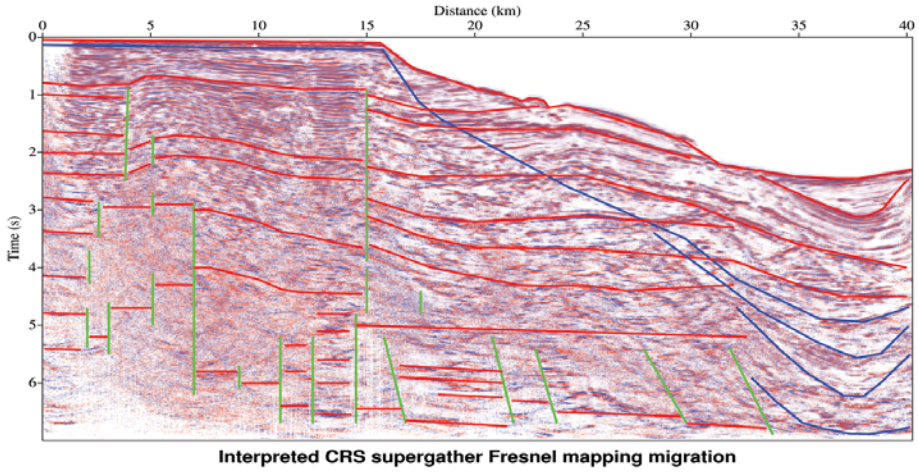


**Figure 21** – The color lines were based on the stack and migration sections. The tracing shows consistent lateral continuation of the reflection events, and also vertical resolution by the separation of the main events.

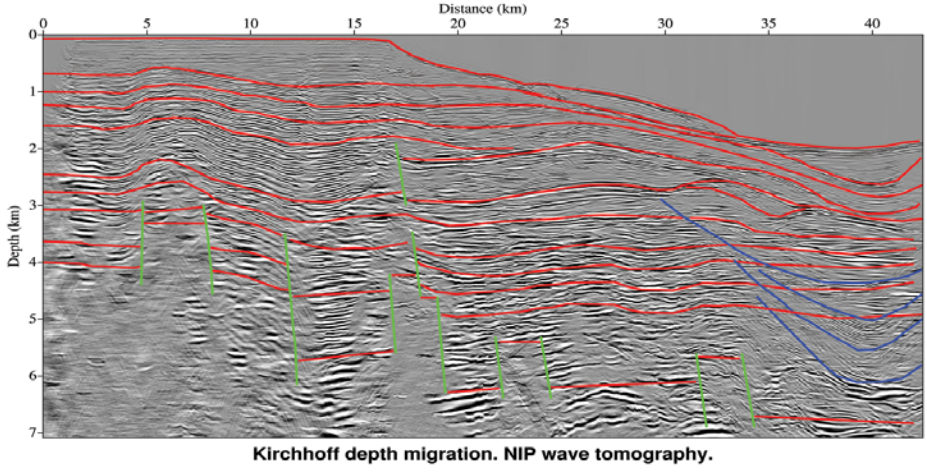


**Figure 22** – Kirchhoff depth migration of Figure 16 with structural interpretation lines, where we used also the information from Figures 20 and 21. The contact sediment/basement/intrusions by the lowest red line, faults in green, reflectors in red also, and multiples in blue. The background was changed to tones of gray for a different visualization.

The coherence measured through the color scales of Figures 17, 18 and 19 show a systematic increase of the process as organized in the flowchart of Figure 1. These figures show the improved resolution as indicated by the visual signal-to-noise ratio and reflector continuity. The interpretation lines intended to separate the different patterns of the seismic events, where is clear the strong geometrical correlation between coherence and attribute sections.

We now turn to Figure 22 presented in gray scale, that has a strong vertical exaggeration, and where the lines represent another (almost independent) interpretation of the geological features. The interpretation is still based on figures for the basin published in geological sites and academic books, and for an idealized geological section, the contribution from this interpretation can be used.

The sedimentary section was interpreted based on reflections with higher frequency content, and clear reflector lateral continuity as, for example, on the top and middle of Figure 22. The basement response was interpreted based on the reflections with lower frequency content, and with poor lateral continuity due to the diffraction patterns. The traced red lines serve also to show reflection depth intervals, that can laterally be homogeneous (see top-left), or that can show lateral and vertical heterogeneities (see center-right). The discontinuities are marked by green lines.

Elevations (intrusions and anticlines) are clear in the section, mainly in the left part where we traced a high as representing

the last reflector (theoretical basement). The blue lines are interpreted multiples based mainly on the form, because measuring time needs a complementary model, and the aim are the primary reflections crossing the multiples (conflicting dips).

It is clear the difficulty in tracing reflectors due to the strong multiples present, and also for the multiple attenuation preserving the primaries. The heavy diffraction events limited the tracing of interpretation lines in the bottom-left part of the figure, that can be compared to Figure 20.

## CONCLUSIONS

The analysis directed to the conflicting dip problem indicates that the main events still locally dominate the section in a consistent form, and other strategies are welcome to bring better results, as multiple attenuation.

Other general comments are directed to the sharp delineation of reflections with the CRS stack process (stack and migration), that can aim at the different applications. A future case is to create a geometrical model for the sedimentary sequence, where we can keep the main features of the optimized stack and migrated sections by mapping the time axis into a depth axis under a proposed and controlled velocity model function. With these clear time reflection boundaries, we can trace depth reflector boundaries as a first geometrical-velocity model for use in the prediction of stress variation to locate low pressure zones that can act as natural pumps for oil and gas accumulation (Sibiryakov et al., 2013, 2015a, 2015b).

A basin reevaluation needs a good geometrically interactive tracing of structures to provide a good basis for geological interpretation, and hopefully for a successful drilling.

This study served to reinforce perspectives and intentions on research to further develop the method, like for the dip conflict, the multiple definition and attenuation, velocity analysis, diffraction stack, and model building for sedimentary basin analysis.

## ACKNOWLEDGMENTS

The authors would like to thank the Brazilian institutions UFPA (*Universidade Federal do Pará*), FINEP (*Financiadora de Estudos e Projetos, Rede 1, Fase 5*), and PETROBRAS (*Petróleo Brasileiro S/A*) for the research support, and specifically to the project National Institute of Science and Technology (*Instituto Nacional de Ciência e Tecnologia*, INCT-GP/MCT/CNPq/FINEP). The thanks are extended to CAPES/CNPq for the scholarship of Wildney W.S. Vieira. Special thanks are extended to the Wave Inversion Technology Group (WIT-KIT, Karlsruhe, Germany) for the academic cooperation support. Thanks also to the reviewers for their notable suggestions.

## REFERENCES

AL-CHALABI M. 1992. When least-squares squares least. Geophys. Prosp., 40(3): 359–378.

BARDAN V. 2005. Dealiasing of seismic common midpoint and common offset gathers. First Break, 23: 27–31.

BAYKULOV M & GAJEWSKI D. 2007. Prestack seismic data enhancement with CRS parameters. Annual Report, Wave Inversion Technology Consortium, 11: 50–61.

BERNABINI M, CARRION P, JACOVITTI G, ROCCA F, TREITEL S & WORTHINGTON MH. 1987. Deconvolution and inversion. [S.l.]: Blackwell Scientific Publications. 366 pp.

CAINELLI C & MOHRIAK WU. 1999. Some remarks on the evolution of sedimentary basins along the eastern Brazilian continental margin. Episodes, 22(3): 206–216.

CERVENY V. 2001. Seismic ray theory. Cambridge: Cambridge University Press. 722 pp.

COHEN JK & STOCKWELL JJW. 2005. CWP/SU: Seismic Un*x Release 39 – a free package for seismic research and processing. [S.l.]: Center for Wave Phenomena, Colorado School of Mines.

DUVENECK E. 2004. Tomographic determination of seismic velocity models with kinematic wavefield attributes. Berlin: Logos Verlag.

GAMBOA F. 2003. Characterization and elimination of multiples by the commom reflection surface method (in Portuguese). Doctorate Thesis – UNICAMP, Universidade Estadual de Campinas, São Paulo, Brazil, Faculdade de Engenharia Mecânica, Instituto de Geociências, Out. 2003. 160 pp.

GIERSE G, PRUESSMANN J, LAGGIARD E, BOENNEMANN C & MEYER H. 2003. Improved imaging of 3D marine seismic data from offshore Costa Rica with CRS processing. First Break, 21: 19–23.

GOMES AB, LEITE LWB, SADALA L, PESTANA R, ALDUNATE G & MANN J. 2007. Modelling, stack and imaging: Marine seismic. In: 10th International Congress of the Brazilian Geophysical Society, Rio de Janeiro, Brazil. CD-ROM.

GUPTA HK. 2011. Encyclopedia of Solid Earth Geophysics. Hyderabad, India: Springer. 1578 pp.

HEILMANN BZ. 2007. CRS-stack-based seismic reflection imaging for land data in time and depth domains. Doctorate Thesis – Karlsruhe University, Karlsruhe, Feb. 2007. 177 pp.

HEILMANN BZ, LEITE LWB & GOMES AB. 2007. Basin reevaluation by CRS: stack-based seismic reflection imaging. In: 10th International Congress of the Brazilian Geophysical Society, Rio de Janeiro. CD-ROM.

HUBRAL P. (Ed.). 1999. Macro-model independent seismic reflection imaging. [S.l.]: Elsevier. 209 pp.

HUBRAL P & KREY T. 1980. Interval Velocities from Seismic Reflection Time Measurements. Tulsa, OK: Society of Exploration Geophysicists.

KOGLIN I. 2005. Estimation of residual static time shifts by means of the CRS-based residual static correction approach. Berlin: Logos Verlag. 163 pp.

KOGLIN I, MANN J & HEILMANN Z. 2006. CRS-stack-based residual static correction. Geophysical Prospecting, 54: 697–707.

KRAVTSOV YA & ORLOV YI. 1990. Geometrical optics of inhomogeneous media. Berlin: Springer Verlag. 312 pp.

LEITE LWB, HEILMANN BZ & GOMES AB. 2008. CRS seismic data imaging: A case study for basin reevaluation. Brazilian Journal of Geophysics, Rio de Janeiro, 25(3): 321–336.

MANN J. 2002. Extensions and applications of the Common-Reflection-Surface Stack method. Berlin: Logos Verlag. 187 pp.

MANN J, HUBRAL P, TRAUB B, GERST A & MEYER H. 2000. Macro-model independent approximative prestack time migration. In: 62 Mtg. EAGE Extended Abstracts.

MINATO S, TSUJI T, MATSUOKA T, NISHIZAKA N & IKEDA M. 2012. Global optimization by simulated annealing for common reflection surface stacking and its application to low-fold marine data in southwest Japan. Exploration Geophysics, 43: 59–69.

MOHRIAK WU, SZATMARI P & ANJOS SMC. 2008. Sal: Tectônica e Geologia: Geologia e Tectônica. São Paulo: Editora Beca. 673 pp.

MÜELLER T, JÄEGER R & HÖCHT G. 1998. Common Reflection Surface stacking method – imaging with an unknown velocity model. In: 68th Ann. Internat. Mtg., Expanded abstracts, SEG, p. 1764–1767.

RONEN J & CLAERBOUT JF. 1985. Surface-consistent residual statics estimation by stack-power maximization. Geophysics, Tulsa, OK, 50(12): 2759–2767.

SENGBUSH RL. 1983. Seismic exploration methods. [S.l.]: International Human Resources Developed Corporation. 296 pp.

SHERIFF RE & GELDART L. 1995. Exploration Seismology. Cambridge: Cambridge University Press. 580 pp.

SIBIRYAKOV B, LEITE LWB & VIEIRA WWS. 2013. Model of the structured continuum, and the relation between specific surface area, porosity and permeability. Brazilian Journal of Geophysics, 31(4): 559–568.

SIBIRYAKOV BP, LEITE LWB & VIEIRA WWS. 2015a. Behavior of stresses and hydrodynamics from multicomponent seismic data. Brazilian Journal of Geophysics, 33(1): 57–70.

SIBIRYAKOV B, LEITE LWB, SIBIRYAKOV EP & VIEIRA WWS. 2015b. Local low pressure areas in anticline structures Brazilian Journal of Geophysics, 33(2): 225–236.

SILVA DAB. 2012. Processing, Inversion and Imaging of marine seismic data (in Portuguese). Master Dissertation – Universidade Federal do Pará. 187 pp.

SOLEIMANI M, PIRUZ I, MANN J & HUBRAL P. 2009. Solving the problem of conflicting dips in Common-Reflection-Surface (CRS) stack. In: 1st Internat. Conf. & Exhib., Extended Abstracts, Shiraz, Iran, EAGE.

TARANTOLA A. 2005. Inverse problem theory and methods for parameter estimation. [S.l.]: SIAM.

TRAPPE H, GIERSE G & PRUESSMANN J. 2001. Case studies show potential of common reflection surface stack-structural resolution in the time domain beyond the conventional NMO/DMO stack. First Break, 19(11): 625–633.

URSIN B. 1982. Quadratic wavefront and traveltime approximations in inhomogeneous layered media with curved interfaces. Geophysics, Tulsa, OK, 47(7): 1012–1021.

VERSCHUUR DJ, BERKOUT AJ & WAPENAAR PA. 1992. Adaptive surface-related multilpe elimination. Geophysics, 57(9): 1166–1177.

Recebido em 16 julho, 2014 / Aceito em 28 maio, 2016
Received on July 16, 2014 / Accepted on May 28, 2016

## NOTES ABOUT THE AUTHORS

**Lourenildo Williame Barbosa Leite** is a Professor of Geophysics in the Undergraduate and Graduate Courses of the Universidade Federal do Pará (UFPA), Brazil. Obtained a Masters and a Doctorate in Geophysics from Saint Louis University, Missouri, USA. Develops research work in applied seismic for oil and gas exploration aiming at velocity analysis towards stack, inversion, migration and attribute analysis. Member of SBGf, SEG, EAGE and SSA societies.

**Juergen Mann** was a Research Assistant at the Karlsruhe Institute of Technology – KIT, Geophysics Institute, Germany. Obtained a Masters and a Doctorate in Geophysics from KIT, former University Fridericiana Karlsruhe. Develops research in applied seismic for oil and gas exploration aiming at velocity analysis, stack and migration under the CRS Technology of WIT – Wave Inversion Technology. Member of SEG and EAGE societies.

**Wildney Wallacy da Silva Vieira** is a Doctorate student at the Graduate Course in Geophysics of the Universidade Federal do Pará (UFPA), Brazil. Obtained a Bachelors in Mathematics (in 2007), and a Masters of Geophysics (in 2011), both degrees at UFPA. Develops research work in seismic methods applied to oil and gas exploration. Area of interest has been ultimately focused at imaging by a complete processing workflow passing by data quality control, velocity analysis, inversion and migration.